SOME PROPERTIES OF Bi_2Te_3 AND PbTe CRYSTALS AND CONVERTERS ON THEIR BASIS

D. F. Meglei

Institute of Electronic Engineering and Nanotechnology „D.Ghitsu”,
Academy of Sciences of Moldova, Academiei str. 3/3, Chisinau, MD 2028, Republic of Moldova
E-mail: meglei@iieti.asm.md

(Received 10 May 2012)

Abstract

Owning to the miniaturization of solid state electronic devices, the problem of studying the physical and physicochemical processes in low-dimensional condensed systems, in addition to scientific interest, is of particular practical significance. In theoretical terms, this is due to the fact that a one-dimensional model has simpler solutions; in the experimental aspect, this is the possibility to obtain highly perfect single crystals, the size effects in which are more severe than, for example, in thin layers, because of two-dimensional limitations. In practical terms, these systems can be used in all modern fields of solid state electronics, because these materials make it possible to solve some problems in instrument engineering related to miniaturization, improving the accuracy and stability, and expanding the range of allowed climatic and mechanical effects. A small diameter of a microwire (MW) ($1 \cdot 10^{-6}$ m) provides a significant reduction in the weight and dimensions of elements made of MWs and decreases their mechanical, thermal, and electrical inertia. A solid insulation protects the core material from the interaction with the environment, which contributes to an increase in the stability, strength, and other parameters of sensors prepared on their basis. Narrow-gap semiconductors, such as lead telluride (PbTe) and bismuth telluride (Bi_2Te_3), are promising materials for thermoelectrics, optoelectronics, and laser technology. Therefore, systems of complex components based on them, in particular, thin films and MWs, have been intensively studied in recent years [1-5], the more so as the problem of production of converters on their basis cannot be considered solved at the moment.

1. Technique for the Preparation of Glass-Insulated MWs

For the first time, thin metal wires in glass insulation were obtained in 1924 using a conventional gas heater [6]. However, this method was not used widely because of the low production efficiency.

Cylindrical single-crystal wire crystals (WCs) of bismuth in glass insulation were prepared by liquid phase casting by the Ulitovsky method [7, 8]. Using this technique, Bi WCs with the diameters of the core and glass insulation ranging from a few tens of fractions to a few tens and hundredths of microns were prepared.

The casting of Bi MWs has several features:

(1) The melting point of Bi is much lower than the softening temperature of glass used for the casting of MWs; therefore, it is necessary to overheat the material to obtain a capillary.

(2) In the experiments, various types of glass (Nonex glass, Pyrex, C37-2, molybdenum glass, etc.) were tested.

(3) The choice of the glass–material pair for the formation of MWs plays an important role for

the successful casting of MWs. The adhesion between the material and the glass is very important, because the melt is drawn by a moving capillary only in the interaction between the material and the glass. Good adhesion of Bi and glass is provided by the presence of a thin oxide film on the surface of molten Bi.

(4) Experiments and calculations show that the mass of Bi after melting is suspended only due to the ponderomotive forces of the electromagnetic field of the inductor (the critical mass is 0.4-0.8 g). This is explained by the low capillary constant and high electrical resistance of bismuth. Despite this, owning to the existence of relatively viscous glass insulation, it is possible to draw a microwire from a droplet whose mass is much higher than critical. The shape of a Bi droplet differs from conventional; it has a shape of a bulb with the top directed downward to the capillary.

(5) A sharp temperature decrease along the height of the droplet is observed at 300-400°C; as a result, its upper part is located in a less intense electromagnetic field. In connection with this circumstance, the melt in the upper part of the droplet is additionally suspended due to the interaction with the glass insulation, which is more viscous. This explains the above methods [7] for high-speed drawing of masses higher than the critical one.

The totality of the above factors makes it possible to prepare bismuth MWs that are more uniform along the axis than metal ones.

By controlling the temperature of the droplet, the capillary drawing rate, and the ampoule lowering rate, it is possible to obtain fairly long WCs with different diameters.

Later on, the technique for preparing glass-insulated MWs from various semiconductor materials with necessary physical parameters, such as bismuth telluride (Bi_2Te_3), lead telluride (PbTe), Bi doped with different impurities, was optimized.

The crystallization of MWs occurs due to supercooling at the solid-melt interface (the cooling rate is about 10^5-10^6 deg/s). The value of supercooling is characterized by the expression

$$\theta_{min} = (\lambda \kappa)^{-1} (\varepsilon/\kappa)^{\varepsilon/2g} [(2 \lambda g \theta_{nn} - \gamma v g) / (\gamma v g)^{\varepsilon/\kappa}]^{\kappa/2g},$$

where $\varepsilon = v^2 / 2a - [(v^2 / 4a^2 + 2 \alpha / \lambda R)]^{1/2}$;

$$\kappa = v / 2a + [(v^2 / 4a^2 + 2 \alpha / \lambda R)]^{1/2};$$

$$g = [v^2 / 4 a^2 + 2 \alpha / \lambda R]^{1/2}.$$

Here λ is the thermal conductivity, *a* is the temperature conductivity, α is the heat transfer coefficient, θ_{nn} is the melting temperature, γ is the density, R is the core radius, and *v* is the rate of casting.

Supercooling and high rates of crystallization lead to the growth of a single-crystal core of MWs.

The results of studies of the resulting MWs showed that, along the length of MWs prepared from different materials, there are many breaks, which do not depend on the type of the used glass. The main causes of their occurrence are the high rate of their crystallization and the different temperature coefficient of linear expansion of the material and the glass. The high rate of crystallization contributes to the supercooling in the melt, which results in the formation of spontaneous crystallization centers, which contribute to the appearance of new centers of crystallization. The melt in a glass capillary is located between two crystallization centers, which are attracted to each other during crystallization, which leads to the formation of microcracks in

MWs.

In addition, during the formation of MWs, due to the evaporation of the molten material, the vacuum pressure over it decreases, which also leads to the formation of microcracks. Therefore, to prepare MWs of PbTe (Fig. 2), we used the method of filling glass capillaries under an inert gas pressure; for Bi_2Te_3, we used an evacuated and hermetically sealed tube. In the latter case, we adapted the setup for casting by the Ulitovsky method; that is, we replaced the inductor by a resistance furnace with a stabilized temperature [4, 9].

The quality of the resulting MWs was estimated visually using a NEOPHOT-30 microscope and studying the microstructure of longitudinal sections. The analysis revealed a number cracks along the length of the MWs, which are caused by the high rate of crystallization and the different coefficient of thermal expansion of the material and the glass. These microcracks are removed by zone recrystallization.

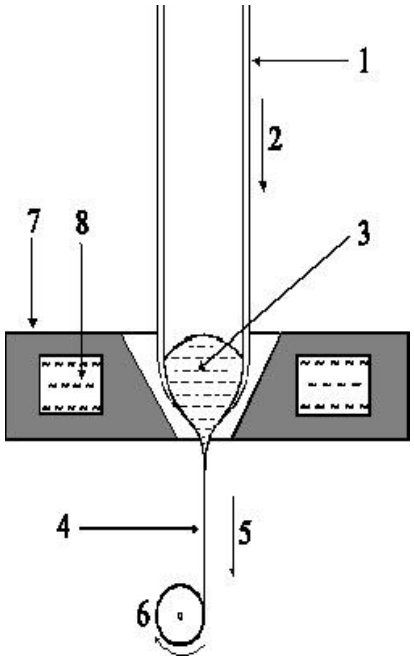

Fig. 1. Schematic representation of the setup for drawing MWs by the Ulitovsky method: (1) glass tube, (2) direction of movement of the tube, (3) liquid material, (4) MW in glass insulation, (5) direction of MW, (6) MW receiving unit, (7) high-frequency inductor, and (8) water for cooling the inductor.

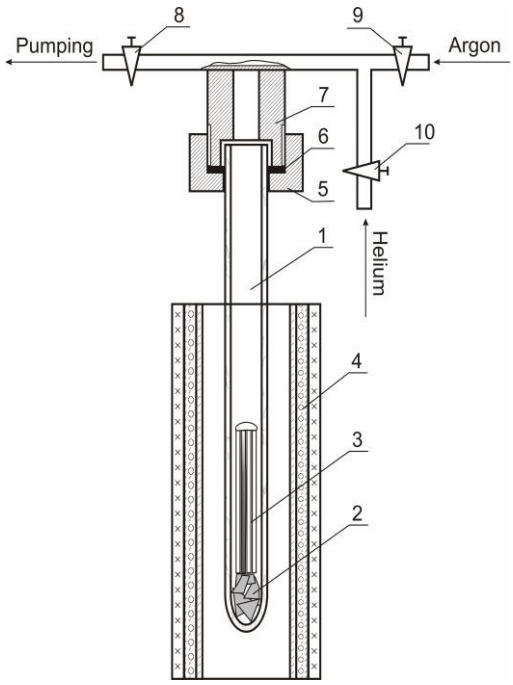

Fig. 2. Diagram of a setup for the preparation of MWs under an inert gas pressure: (1) quartz tube, (2) PbTe material, (3) quartz capillary, (4) electric furnace, (5) screw, (6) gasket, (7) bushing, (8, 9, 10) vacuum valves.

The highest quality PbTe MWs are obtained by filling quartz glass capillaries with the material under an inert gas pressure; the method is as follows: evacuated quartz tube *1* (Fig. 2) with weighted material *2* and dead-end quartz capillaries fixed above it are loaded into high-temperature furnace *4* in such a way that the capillaries and the material are in the working zone of the furnace (at a temperature above the temperature of the liquid material). After melting of the material and immersion of the capillaries into the molten material, an excess pressure of

$P = (2\text{-}12) \cdot 10^2$ Torr is formed in the tube due to an inert gas; as a result, the capillaries are filled with the melt. Subsequently, the directional crystallization of the melt occurs inside the capillaries.

The disadvantage of this method is that the WC length is on the order of 3–5 cm.

2. Preparation of a Bifilar MW

The preparation of a bifilar MW is similar to that of an MW with a single core and a coaxial MW. To obtain a bifilar MW, we use two glass tubes with a diameter of 5-6 mm sealed on one side; a few grams of a metal, semimetal, or semiconductor material in the form of small granules are placed into the tubes. After evacuation to a pressure of 10^{-5} Torr, they are soldered to one another as shown in Fig. 3.

Here, tube *1* is filled with granular material *2*; another tube *3* is filled with another granular material *4*. The resulting double tube is placed into a heated resistive furnace, in which the materials in the two tubes melt, and the tube glass softens. Next, using a glass rod, we come in contact with the lower end of the softened tubes; a part of glass is drawn into two capillaries, which are bifilar soldered and filled with different materials, and is wound, using a special receiver, in the form of a single bifilar MW in glass insulation with two electrical conductors insulated from one another.

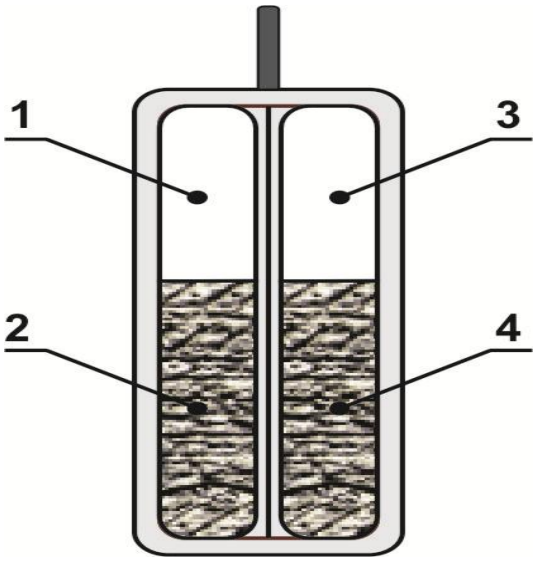

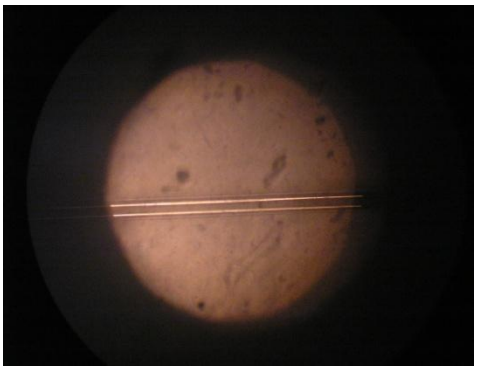

Fig. 3. Tubes for the preparation of a bifilar MW. **Fig. 4.** Segment of a bifilar MW.

Depending on the temperature of the furnace, the rate of lowering the tube in the furnace, and the drawing rate of the MW, we can prepare MWs with various diameters.

Figure 4 shows, as an illustration, a segment of a bifilar MW of semiconductor thermoelectric materials. Here (Fig. 3) *1* and *3* are glass insulation; *2* and *4* are conductive electrodes of a thermoelectric material of *n*- and *p*-type conduction.

We shall describe the example of the preparation of a bifilar MW from bismuth telluride thermoelectric material with *n*- and *p*-type conduction.

In tube *1* (Fig. 3) with an outer diameter of 4-5 mm, we load 4-5 g of bismuth telluride of the *n*-type conduction; in tube *3* with the same diameter, we place the bismuth telluride material of the *p*-type conduction with the same weight. After evacuation of the double tube, using our facility, we obtain a bifilar MW (Fig. 4) an outer diameter of 20-60 μm and a diameter of conducting electrodes of 10-30 μm depending on the process. Depending on the amount of material, the MW length can vary from 10 m to 100-200 m [11].

3. Thermoelectric Properties of PbTe MWs

Crystal MWs of PbTe of the *n*-type conduction were prepared using original materials in the form of a chemical compound with excess lead with respect to the stoichiometric composition, and with excess tellurium for the *p*-type [12].

Studies of the temperature dependence of the electric conductivity of the MWs based on PbTe of *n*- and *p*-type conduction (Figs. 5 and 6, respectively) in a temperature range of 80-350 K showed the following:

- The electric conductivity σ is metallic; it decreases with increasing temperature; in addition, the intrinsic conductivity is not observed in the temperature range under study.
- The electric conductivity σ depends on the diameter of the MW and increases with decreasing diameter.

The increase in σ with decreasing diameter can be explained as follows. For charge carriers of *n*- or *p*-type, the relation between σ, carrier concentration, and mobility μ can be expressed as

$$\sigma_{p,n} = e\,p(n)\,\mu_{p,n}\,.$$

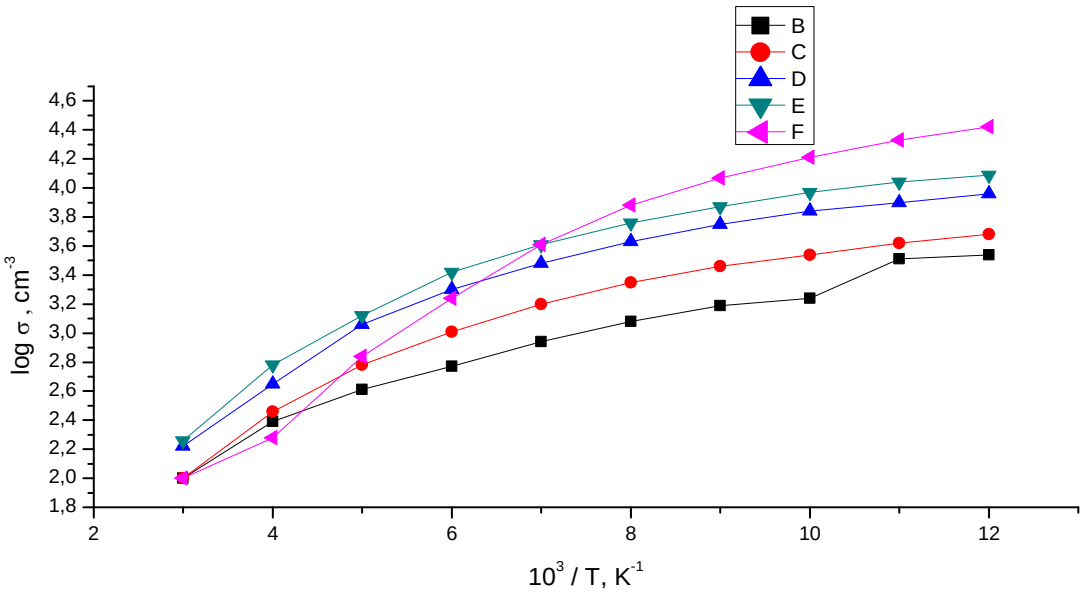

Fig. 5. Temperature dependence of MWs of *n*-type conduction: (B) d = 125.0 μm; (C) d = 92.0 μm; (D) d = 51.0 μm; (E) d = 33.0 μm; (G) d = 15.0 μm; (F) n = 1.2 · 10^{18} cm^{-3} at T = 77 K.

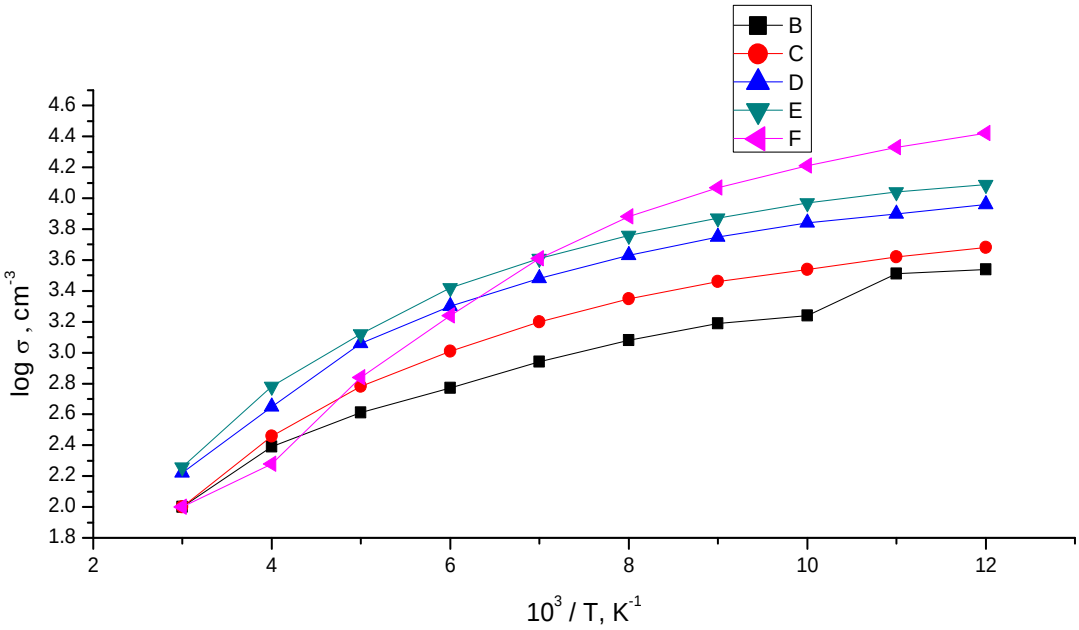

Fig. 6. Temperature dependence of MWs of *p*-type conduction: (B) d = 103.0 μm; (C) d = 45.0 μm; (D) d = 29.3 μm; (E) d = 17.8 μm; (F) p = 1.47 · 10^{18} cm^{-3} at T = 77 K.

It follows from the expression for $\sigma_{p,n}$ that its increase can be caused by an increase in the concentration of p (n) or mobility $\mu_{p,n}$. Studies of the temperature dependence of the thermopower of MWs of various diameters showed (Figs. 7 and 8, respectively) that the thermoelectric coefficient $\alpha_{p,n}$ remains almost unchanged with decreasing diameter of MW.

The expression for coefficient α

$$\alpha_{p(n)} = \pm k/e \, [\, A + ln \, (2(2\pi m_{p(n)} kT)^{3/2} / p \, (n) \, h^3 \,) \,]$$

suggests that the charge carrier concentration p (n) in the studied samples does not depend on the diameter of the MW; hence, the increase in the conductivity σ depends on the increase in the charge carrier mobility. Therefore, the increase in the mobility with decreasing diameter is indicative of an improvement of the structure and homogeneity of MWs with decreasing diameter.

If we compare the results of measurements of σ and α of MWs and bulk crystals, we can conclude that the values of σ and α of the MWs range within the values of the physical parameters of bulk crystals grown by the Bridgman method. This means that the resulting MWs exhibit the same properties as bulk crystals.

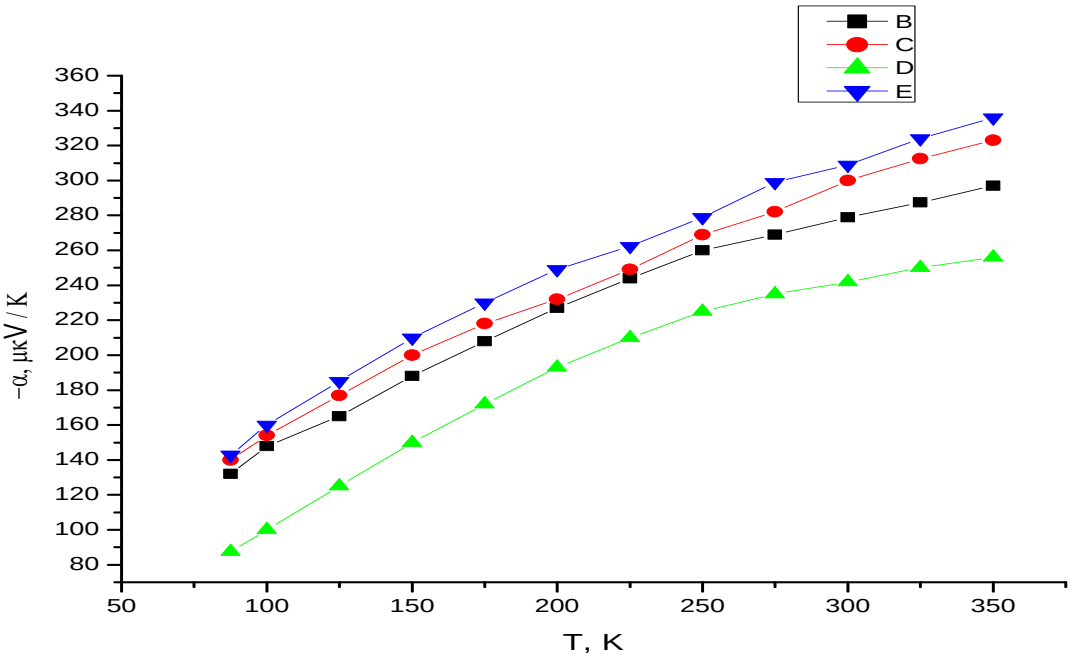

Fig. 7. Temperature dependence of the thermopower of MWs of *n*-type conduction: (B) d = 125.0 μm; (C) d = 51.0 μm; (E) d = 15.0 μm; (D) n = $1.2 \cdot 10^{18}$ cm^{-3} at T = 77 K.

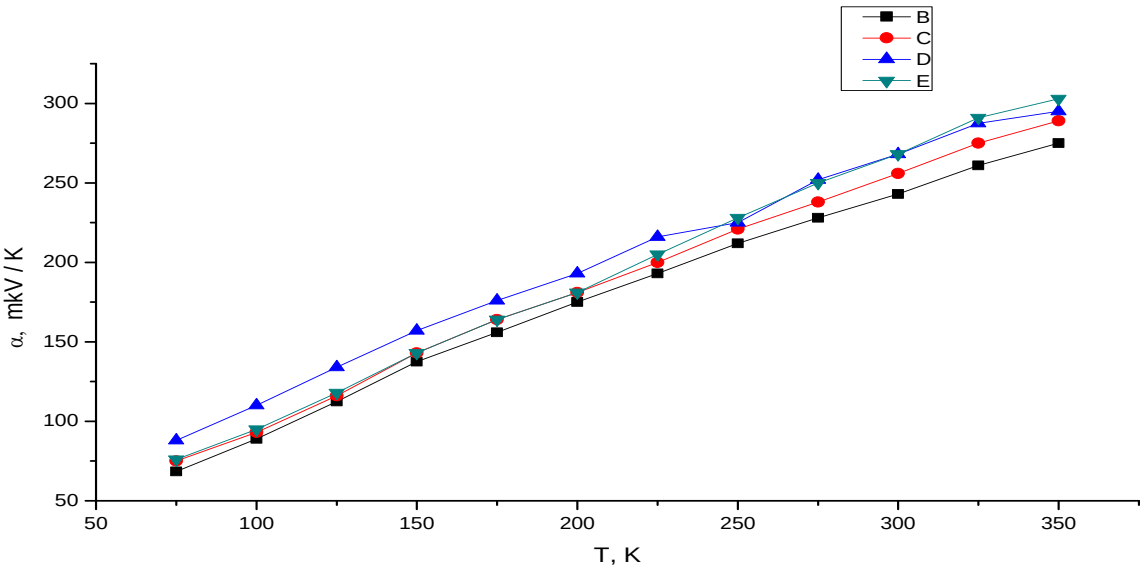

Fig. 8. Temperature dependence of the thermopower of MWs of *n*-type conduction: (B) d = 103.0 μm; (C) d = 45.0 μm; (D) d = 17.8 μm; (E) p = $1.47 \cdot 10^{18}$ cm^{-3} at T = 77 K.

4. Thermoelectric Properties of MWs Based on Bismuth Telluride

The electric and thermoelectric properties were measured using a conventional technique for samples with a length of 5-7 mm cut from different parts of the MW.

The study of the dependence of physical parameters on the process conditions for MWs showed that the thermoelectric coefficient α for the samples of the hole *p*- or electron *n*-conduction at 300 K are in the range, respectively:
$\alpha_p = +(150 \div 300)$ μV/K; $\alpha_n = -(100 \div 140)$ μV/K; $\rho_p = (1 \div 7) \bullet 10^{-3}$ Ω•cm; $\rho_n = (1 \div 3) \bullet 10^{-3}$ Ω•cm [13].

To improve the MW parameters, we performed enormous work on their annealing at different temperatures and duration. The results of the treated samples are shown in Figs. 9-12.

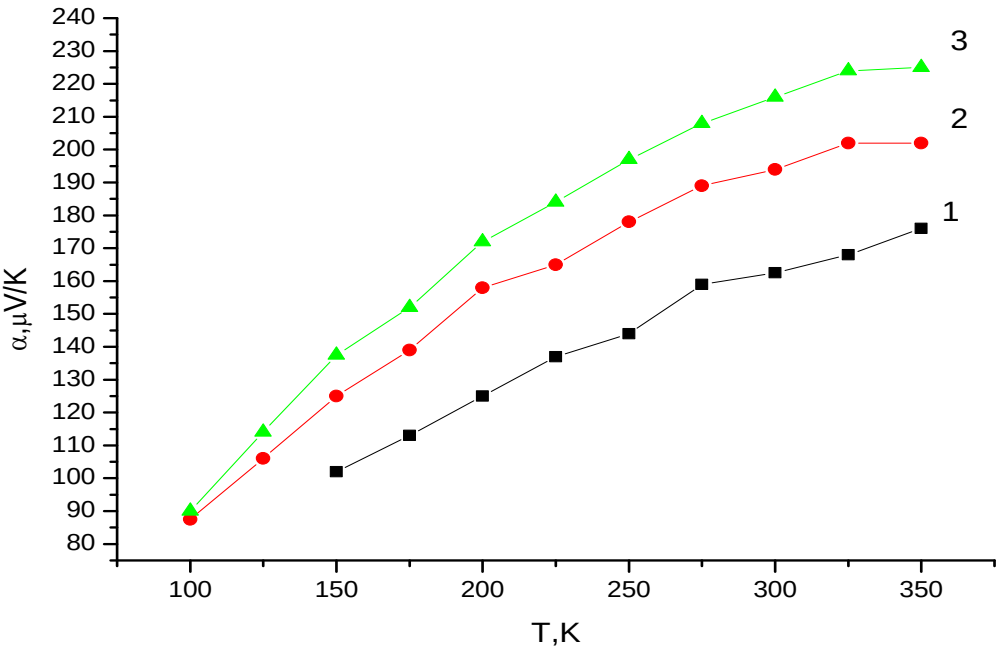

Fig. 9. Temperature dependence of the thermoelectric coefficient of the *p*-type samples: (1) before treatment, (2) after treatment, (3) samples treated at 473 K. The annealing time is 24 h.

These figures show that the isothermal annealing increases both thermopower and resistivity in the samples of the hole conduction; the higher the temperature and annealing time, the higher their parameters.

The results for samples of *n*-type are shown in Figs. 12 and 13. It is evident from the figures that, unlike *p*-type, the resistivity decreases after annealing.

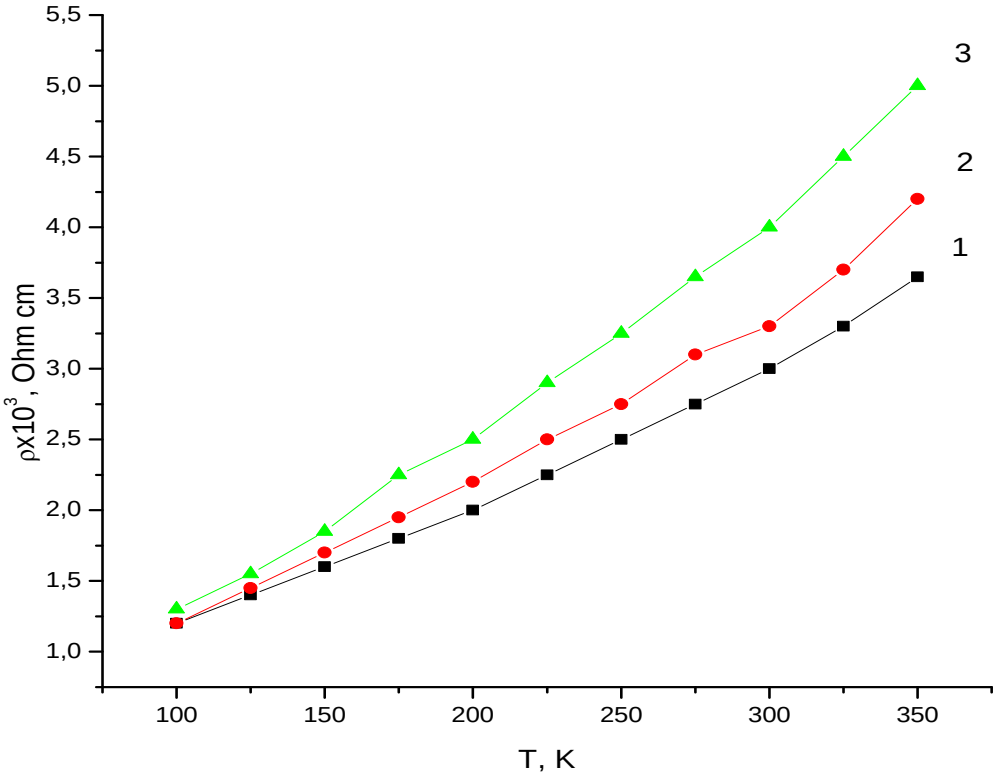

Fig. 10. Temperature dependence of the resistivity of the *p*-type samples: the notation is the same as in Fig. 9.

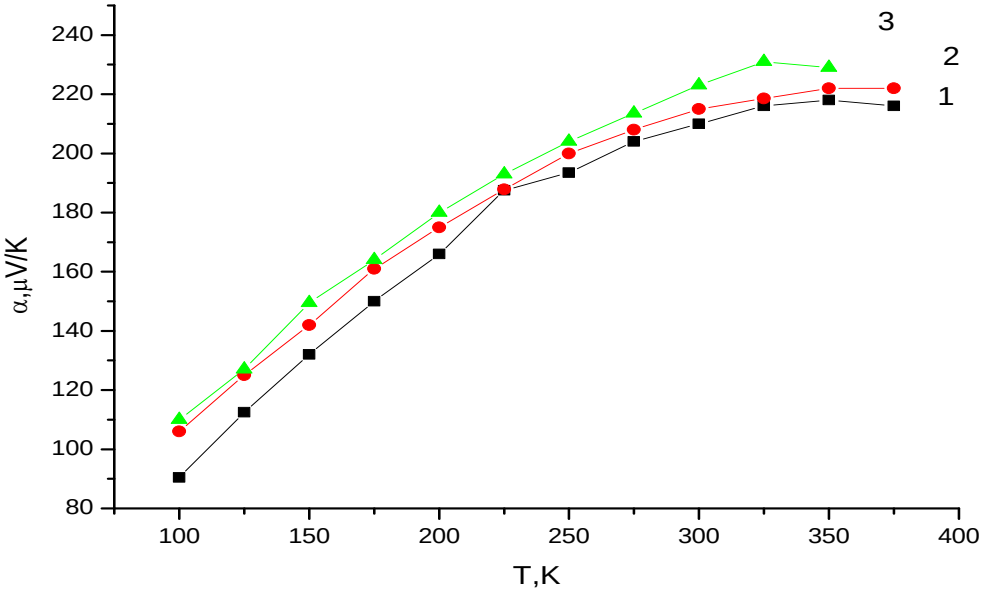

Fig. 11. Temperature dependence of the thermoelectric power of *n*-type samples treated at 450 K in the time interval of (1) 48 h, (2) 96 h, and (3) 73 h.

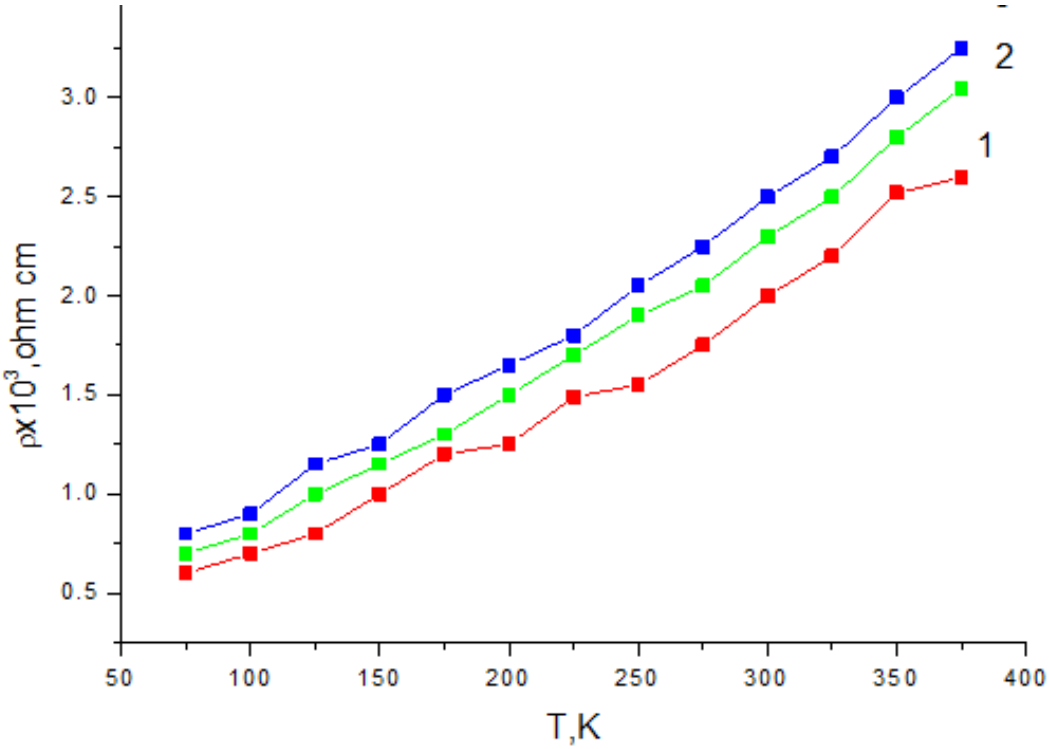

Fig. 12. Temperature dependence of the resistivity of *n*-type samples treated at 450 K in the time interval of (1) 1 h, (2) 72 h, and (3) 96 h.

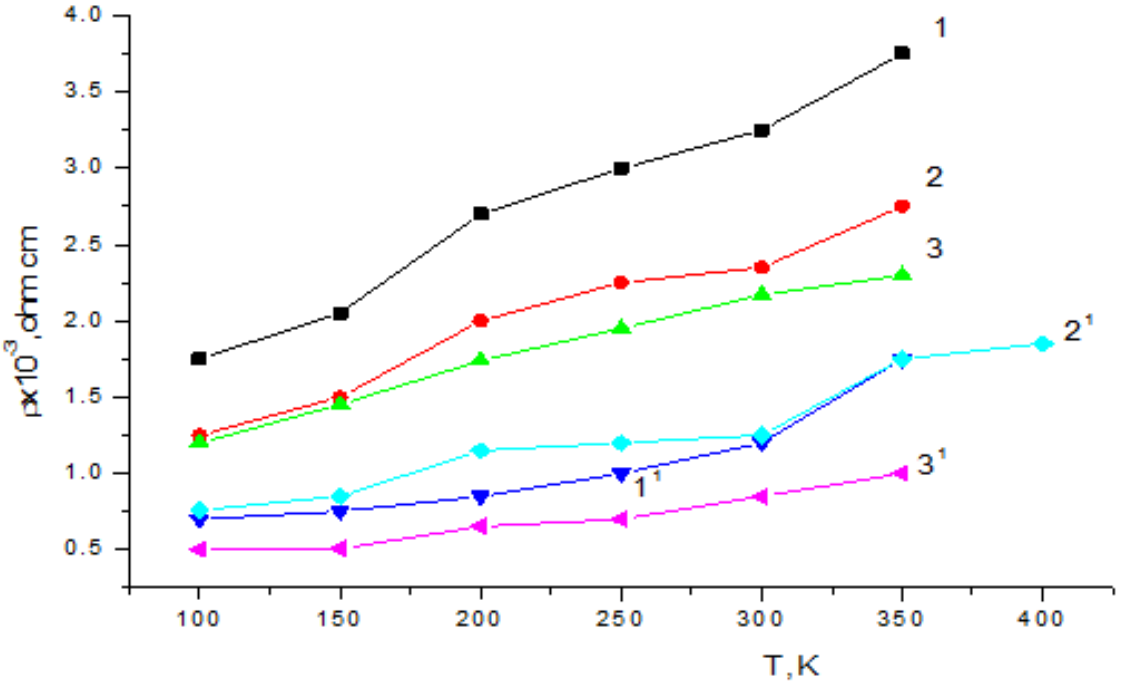

Fig. 13. Temperature dependence of the resistivity of *n*-type samples: (1, 2, 3) untreated and (1', 2', 3') treated.

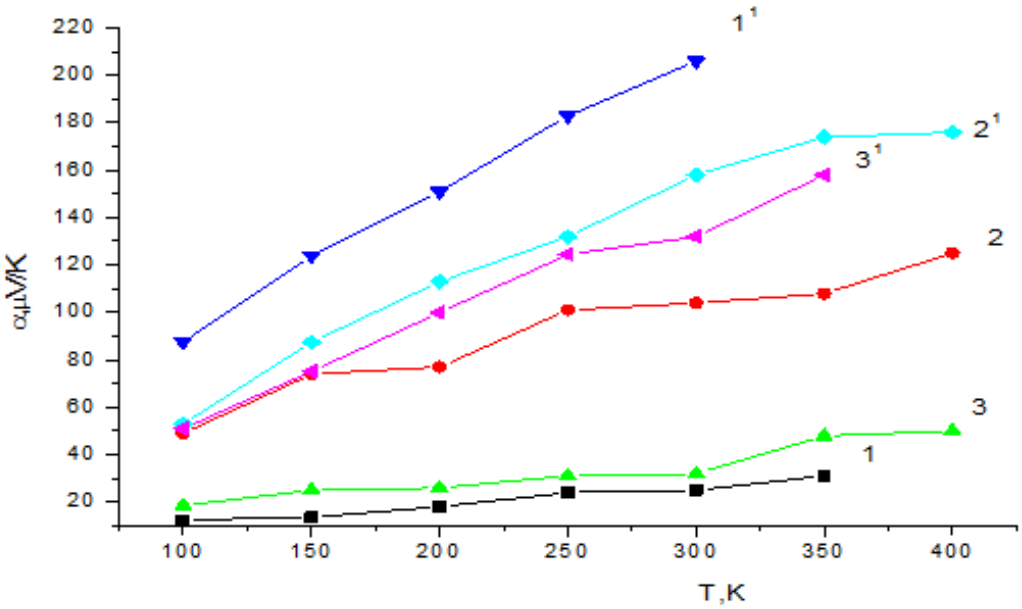

Fig. 14. Temperature dependence of the thermoelectric coefficient of *n*-type samples: (1, 2, 3) untreated and (1', 2', 3') treated.

The change in the annealing temperature of MWs leads to a shift of the maxima in the temperature dependence of thermopower to the range of lower temperatures, which is attributed to the occurrence of intrinsic conductivity at lower temperatures.

To perform aging tests, we used MWs of the two types of conduction before and after annealing for different temperatures and time of annealing. Prior to treatment, we measured resistivity and thermopower. The samples were tested at a temperature of 70°C for 60 h; after that, the samples were stored at room temperature for a month. After the measurement of parameters, the samples were subjected to repeated thermal annealing at 100°C for 40 h; after that, they were stored at room temperature for two months. The results of measurements showed an increase in the parameters after the aging test for untreated MWs and an insignificant change in the treated samples. Therefore, we recommend treating MWs at required temperatures before using in converters.

5. Thermal Efficiency of MWs

According to the theory of thermoelectricity, the efficiency of material of the thermoelectric branches is determined by the quantity

$$Z = \alpha^2\sigma/\kappa,$$

where Z is the thermal efficiency, α is the thermopower, σ is the electric conductivity, and κ is the heat conductivity of the material. The formula shows that it is proportional to $\alpha^2\sigma$ and inversely proportional to κ. Based on this, we shall further discuss in more detail the behavior of the parameter $\alpha^2\sigma$, i.e., the so-called thermoelectric power. Figures 15 and 16 show the temperature dependence of thermoelectric power for the MW of the *n*-type (Fig. 15) and *p*-type (Fig. 16). The calculation showed that, if we assume that the heat conductivity of the MW is equal to that of bulk crystals, then, at 300 K, the thermal efficiency of the PbTe material is $Z = 0.7 \cdot 10^{-3}$ K^{-1}.

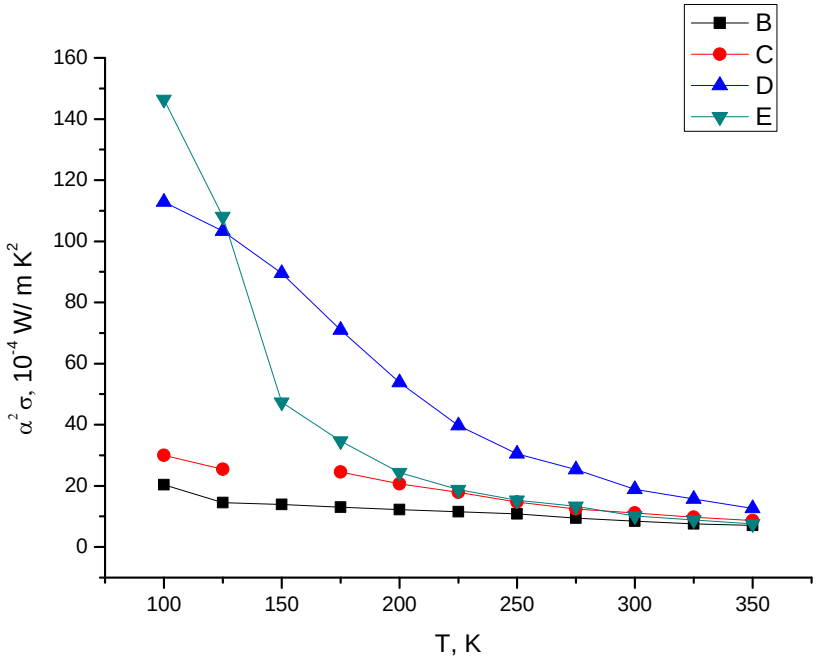

Fig.15. Temperature dependence of the thermoelectric power of *n*-type PbTe MWs: (B) d = 125.0 μm; (C) d = 51.0 μm; (D) n = 1.2 · 10^{18} cm^{-3} at 77 K; (@E) d = 15.0 μm.

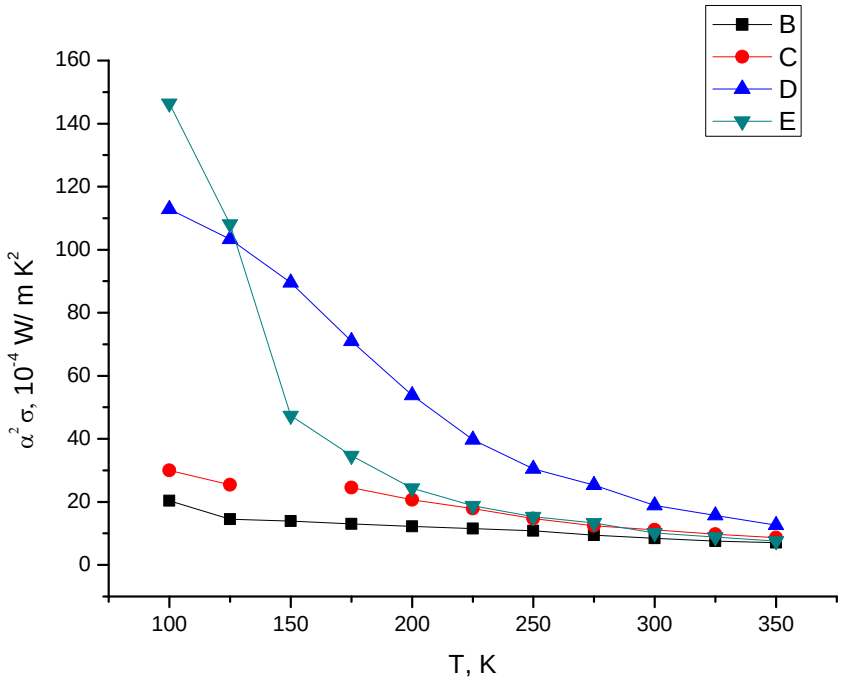

Fig. 16. Temperature dependence of the thermoelectric power of *p*-type PbTe MWs: (B) d = 103.0 μm; (C) d = 45.0 μm; (E) p = 1.47 · 10^{18} cm^{-3} at 77 K; (D) d = 17.8 μm

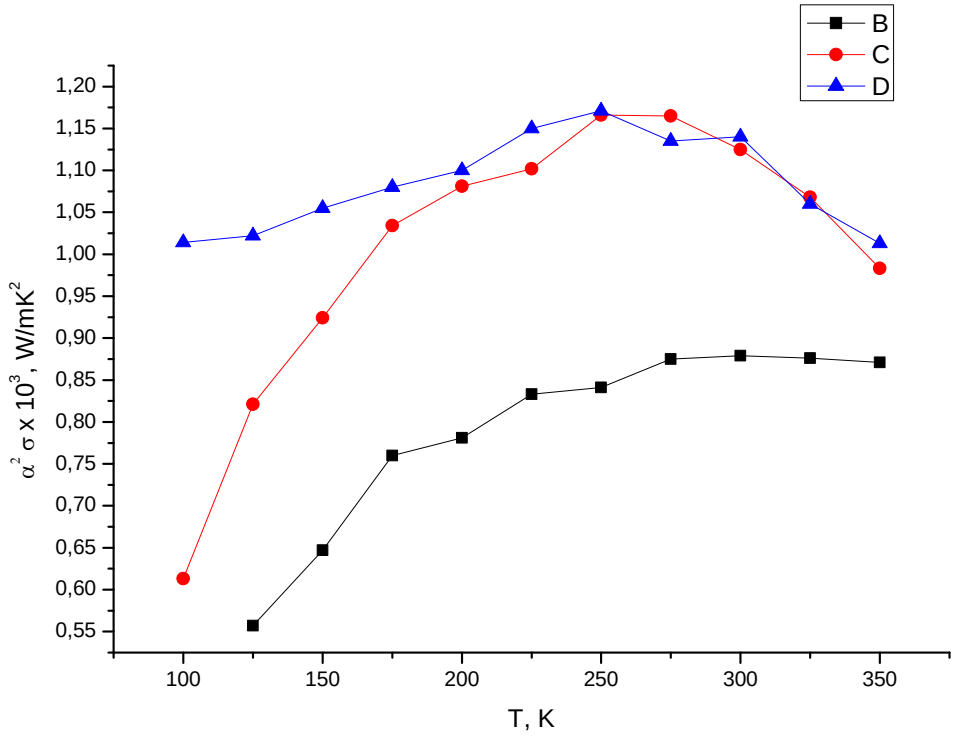

Fig. 17. Temperature dependence of the thermoelectric power of *p*-type Bi_2Te_3 MWs: (B) before treatment; (C) treated at 473 K; (D) treated at 520 K for 24 h.

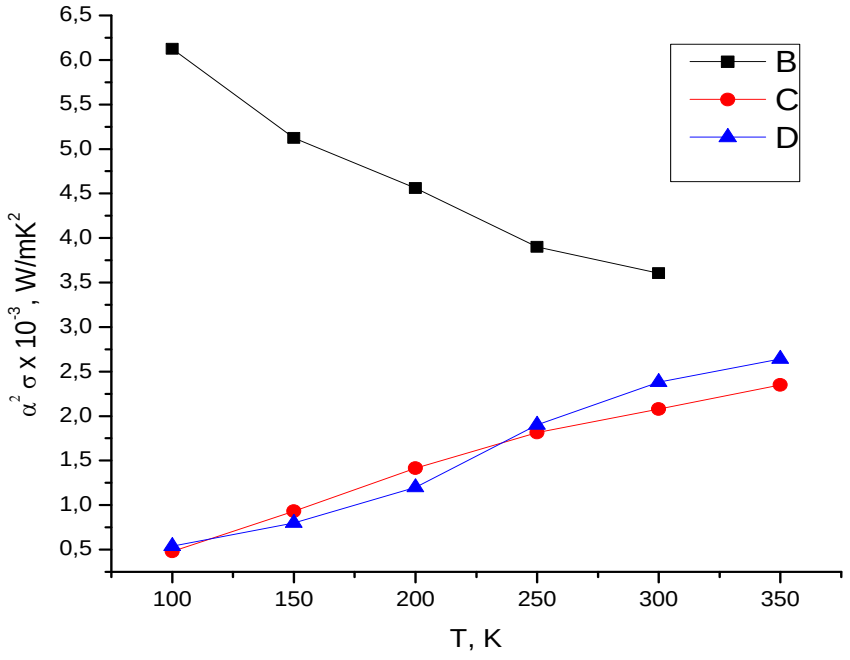

Fig. 18. Temperature dependence of the thermoelectric power *p*-type Bi_2Te_3 MWs: the notation is the same as in Fig. 17.

The thermal efficiency of the Bi_2Te_3 samples of *p*-type conduction at 300 K is $ZT = 0.24$; for *n*-type samples $ZT = 0.51$.

6. Converters Based on Glass-Insulated MWs Infrared (IR) Detectors Based on PbTe Wires

Owing to the diffusion of lead, *p*-n junctions were formed on the resulting *p*-type PbTe WCs. The current-voltage characteristics (CVCs) of the *p*-n junctions were measured for the samples placed in evacuated glass Dewar vessels and cooled by liquid nitrogen to a temperature of 80 K.

Figure 19 shows the CVCs of *p*-n junctions for different wire diameters. It is evident that the reverse branches are characterized by low values of saturation current, which begins to rise at biases greater than 1.5 V. The shape of the forward branches of CVCs heavily depends on wire diameters, a decrease in which leads to an increase in series resistance and to a deviation of the CVC from an ideal dependence. The forward CVC branch in a voltage range of 0.02-0.076 V exhibits a region of an exponential change in current with voltage, which is characteristic of the recombination nature of current. The dynamic resistance at zero bias is in a range of $(1.5–5) \cdot 10^5$ Ω.

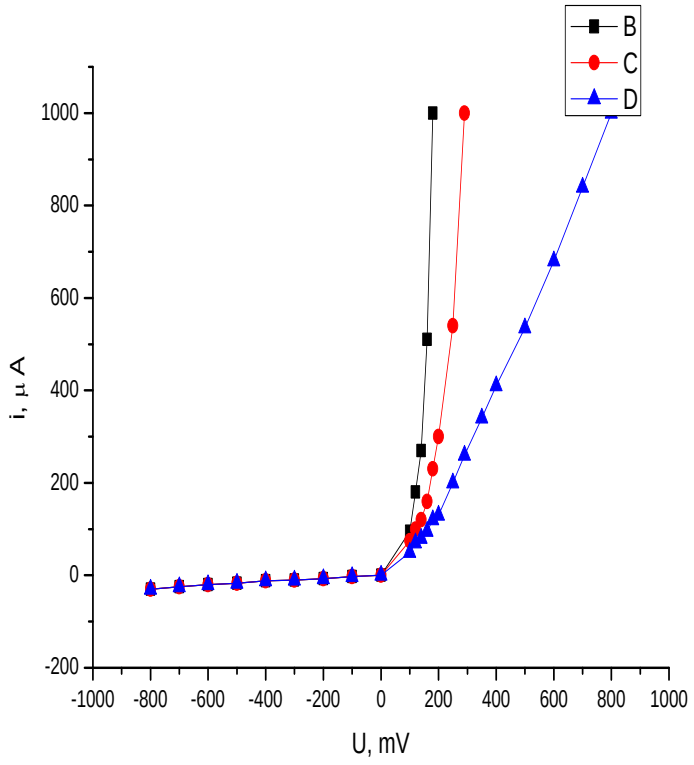

Fig. 19. Current-voltage characteristics of *p*-n junctions: (B) d = 73.3 μm; (C) d = 41.0 μm; (D) d = 33.0 μm.

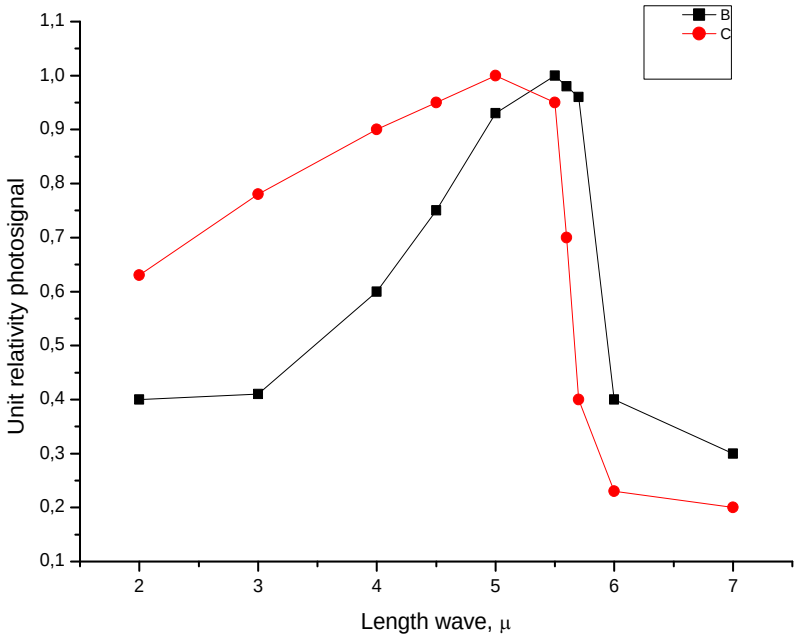

Fig.20. The spectral characteristics of IR detectors.

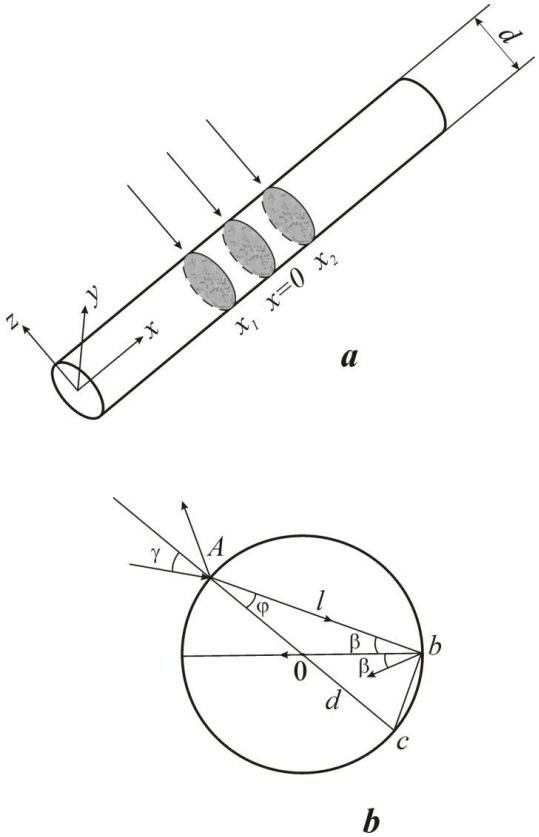

Fig. 21. (a) Geometry of the *p*-n junction and (b) incident radiation propagation paths in it.

The measurement of the CVCs of *p*-n junctions made it possible to estimate the charge carrier concentration in *p*- and *n*-regions of the sample. It was found that, for a sample with a thickness of 40 μm, the electron concentration in the *n*-type region is $N_d = 7.4 \cdot 10^{23}$ cm^{-3}, while for the *p*-type region $N_p = 3 \cdot 10^{24}$ cm^{-3}.

The spectral characteristics of IR detectors are depicted in Fig. 20, which shows that the sensitivity of the detectors has a peak before the long-wavelength limit, which is determined by the band gap. The maximum sensitivity of the measured diodes was about 10^5 V/W at 80 K.

Figure 21 shows the geometry of the *p-n* junction and the travel paths of the incident radiation in a sample with a circular cross section. For this geometry of the propagation of incident radiation, in the calculation of absorption, we must take into account multiple reflections of the beam from the back wall of the sample and the effect of the cylindrical lens of the radiation detector.

This analysis for PbTe is fairly simple, because the refractive index of these single crystals is high (n = 5.64) [14]. It is readily seen from the Fig. 21b that the chord length l along which the beam propagates is almost equal to the diameter of the sample. In fact, the ABC triangle show that $\sin\varphi = (1/n)\sin\gamma$. Since the angle γ can take values of 0 to 90°, the maximum difference of l from d is ~1.7% ($l = d\cos\varphi$). Thus, accurate to 2%, $l = d$ for any incidence in the range $0 \le \gamma \le 900$ and all subsequent multiple internal reflections occur along the chord $l = d$; the generation of charge carriers in the cylindrical sample is similar to samples with a square section whose width and thickness are equal to l. Thereupon, according to [15], the rate of carrier generation

$$g = [\ \eta\alpha I(1-R_s)/h\nu\ ]\ (\ 1-e^{-\alpha d}\ )/\ (\ 1-R_s\ e^{-\alpha d}\ ).$$

The short-circuit photocurrent for the case of the absence of surface generation is as follows:

$$i_\phi = (e^2\mu_n N_d\tau_e S/\varepsilon\varepsilon_0)\int_0^{x1}[\ g(x)\,dx + e^2\ \mu_p N_p\tau_p S/\varepsilon\varepsilon_0\ (\ \int_0^{x2}\ g(x)\,d(x)\ ].$$

Here μ_n and μ_p are the mobilities of electrons and holes, N_d and N_p are the carrier concentrations, τ_e and τ_p are carrier lifetimes, ε = 400 is the dielectric constant, and S is the area of the p-n junction. Since the absorption coefficient α is a function of electric field E and photon energy $h\nu$, the integration of the last expression is rather complicated. According to the Poisson equation [15]

$$E = -\ e\ N_d\ (\ x - x_1\ )\ /\ \varepsilon\varepsilon_0 \quad \text{at } x_1 \le x \le 0 \quad \text{and}$$
$$E = \ \ e\ N_p\ (\ x - x_2\ )/\ \varepsilon\varepsilon_0 \quad \text{at } 0 \le x \le x_2,$$

the problem is significantly simplified.
If the photon energy is higher than the band gap E_g, for direct allowed transitions, α takes the form [16]

$$\alpha\ = A\ (h\gamma - E_g)^{1/2}[\ 1 - G(h\gamma,E)],\ \text{where}\ A = \pi c^2\ (2m_r)^{3/2}\ E_g/\ (3m_n n\varepsilon_0 c h^3\gamma),$$

according to [17],

$$G(h\gamma,E) = -E_0^{3/2}\cos\ [4(h\gamma - E_g)^{3/2}/(3E_0^{3/2})]/\ 4(h\gamma - E_g)^{3/2}.$$

According to [20], for the saturation current i_s, we have

$$i_s = en_i^2 S/\tau^{1/2}\cdot\{\ D_n^{1/2}\ \mathrm{cth}[l/(D_n\tau)^{1/2}]/\ (N_a - N_d) + D_p^{1/2}\ \mathrm{cth}\ [l\ /\ (D_p\tau)^{1/2}\ ]\ /\ N_d\}.$$

Here n_i is the intrinsic concentration of charge carriers, D_n and D_p are the diffusion coefficients of electrons and holes, and l is the half-width of the p-n junction. Knowing the photocurrent and the saturation current, we can determine the photo-emf of the p-n junction:

$$V = kT/e\cdot\ln(\ i_\phi\ /\ i_s + 1\ ).$$

The calculated value of photo-emf V = 456 mV is in good agreement with experimental data (200-500 mV).

The calculated detectability, which is limited by thermal noise, is

$$D^* = 1/c\, I \cdot (kT/4R_tS_1) \cdot \ln (i_ф/i_s + 1) = 5.6 \cdot 10^{11} \text{ cm Hz}^{1/2}/\text{W}.$$

If we neglect the dependence of α on electric field, the value of photocurrent decreases almost two fold.

Thus, our data show the following. The used geometry of propagation of the incident radiation at the *p-n* junction is more appropriate for the design of IR detectors. In the calculation of their parameters, it is necessary to take into account the Franz-Keldysh effect. The cylindrical form of the *p-n* junction plays the role of concentration of incident beams.

7. Injection Lasers Based on PbTe WCs

Interest in injection lasers in WCs is caused the possibility to prepare an optron pair, i.e., a source and a detector of radiation, in a spectral range of 3-5 μm in one and the same fiber. To prepare the lasers, we used $Pb_{1-x}Gd_xTe$ (x = 0.0005) WCs of *p*-type conduction with resistivity ρ ≈ (3- 6) x 10^{-4} Ω cm at 77 K. We studied the junctions whose plane is parallel to the cylindrical surface of the WC (coaxial). The region of *n*-type conduction was subjected to diffusion annealing at 973 K in an atmosphere of $Pb_{0.51}Te_{0.49}$ for 90 s; the *n*-layer had a thickness of 20 μm and a length of 0.2-0.5 mm. The configuration of the cylindrical diodes and their location on a copper crystal holder are shown in Fig. 22.

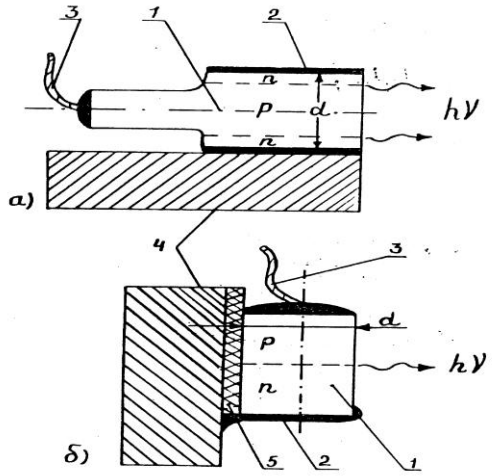

Fig. 22. Configuration of (a) coaxial and (b) transverse laser diodes.

The resistance of the diodes at liquid nitrogen temperature was about 1 Ω. The stimulated emission was measured in a pulse mode at T = 4.2 K. The current pulse duration was 1 μs; the pulse repetition frequency was 170 Hz. The emission spectra were recorded using an IKS-31 monochromator, a detector based on Ge:Au, and a V9-5 stroboscopic converter B9-5.

The threshold current density was 0.1-0.5 kA/cm^2 for the coaxial lasers.

Figure 23 shows the emission spectra of laser diodes with the mode structure in the spectra, which is indicative of lasing.

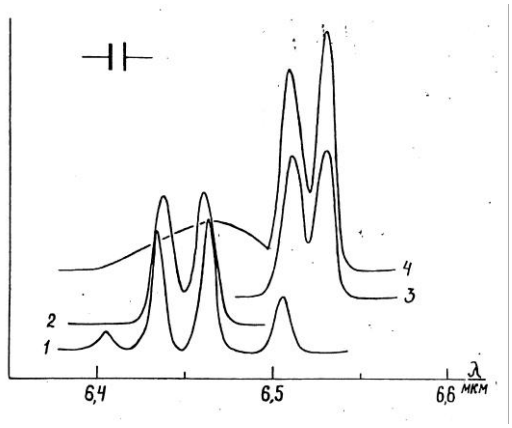

Fig. 23. Emission spectra of (1, 2) transverse and (3, 4) coaxial diodes with different resonator length *l*: d_1 = 120.0 μm, d_2 = 70.0 μm; $l_{3,4}$ = 110.0 μm, d_3 = 56.0 μm, and d_4 = 21.0 μm.

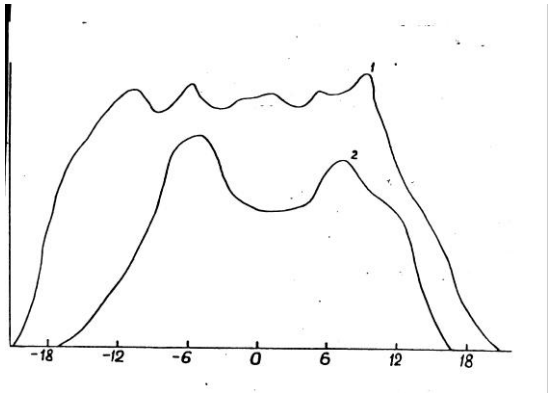

Fig. 24. Directional radiation pattern in the *p*-n junction plane: (1) transverse and (2) coaxial.

The generation of a coaxial diode was observed at a wavelength corresponding to the band gap of PbTe at 4.2 K (Fig. 23, curve *3*). As the length of its resonator *l* decreased, the emission intensity increased, and a wing of spontaneous emission appeared on the short-wave side (Fig. 23, curve *4*). In this case, the mode spacing ($\Delta\lambda \approx 200 - 250$ Å) did not change; that is, it did not depend on the resonator length. The threshold current density slightly increased with decreasing resonator length. These facts indicate that the distribution of current along the wires is inhomogeneous, the mode structure is formed at lengths of the ring *p*-n junction $l \leq 0.2$ mm, and the absorption of radiation (mostly short-wave) occurs on the rest passive part of the crystal.

Figure 24 (curve *2*) shows the directional radiation pattern for a coaxial diode. However, a final conclusion about the spatial distribution of radiation is difficult to make as yet, because the intensity of radiation of the diodes was relatively low. Thus, the results on stimulated emission in the *p*-n junctions in PbTe CWs suggest the possibility of their use as lasers in a wavelength range of 3-6 μm.

8. Microthermocouples

The studied bifilar MW was used as a basis for the preparation of microthermocouples to measure the temperature of various solid, liquid, gaseous, and biological objects by a contact method.

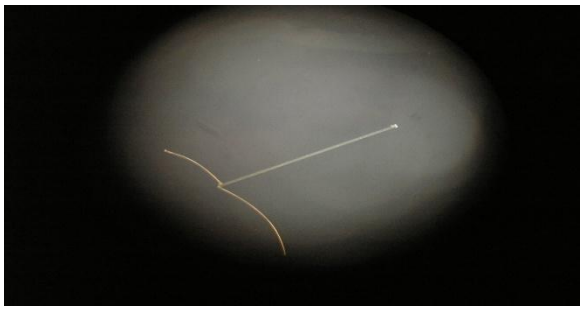

Fig. 25. Microthermocouple based on a bifilar MW.

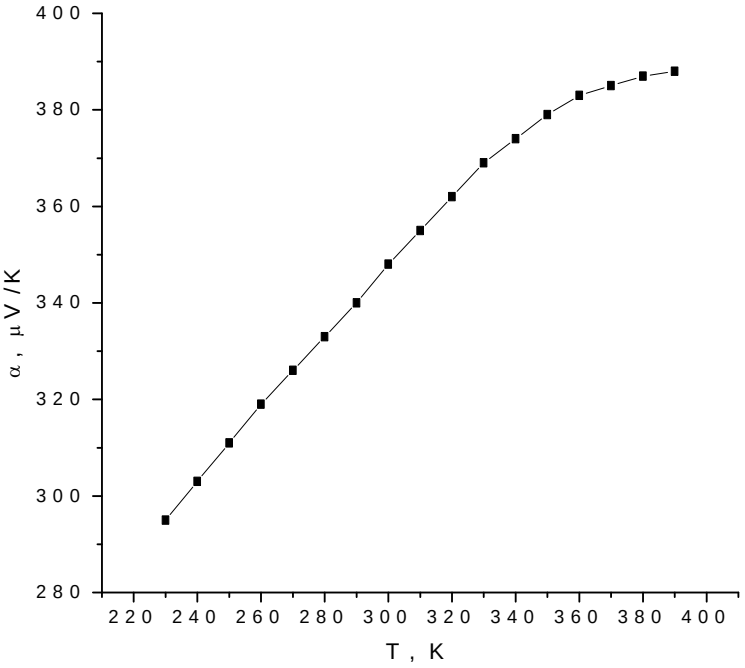

Fig. 26. Temperature dependence of the thermoelectric power of the thermocouple.

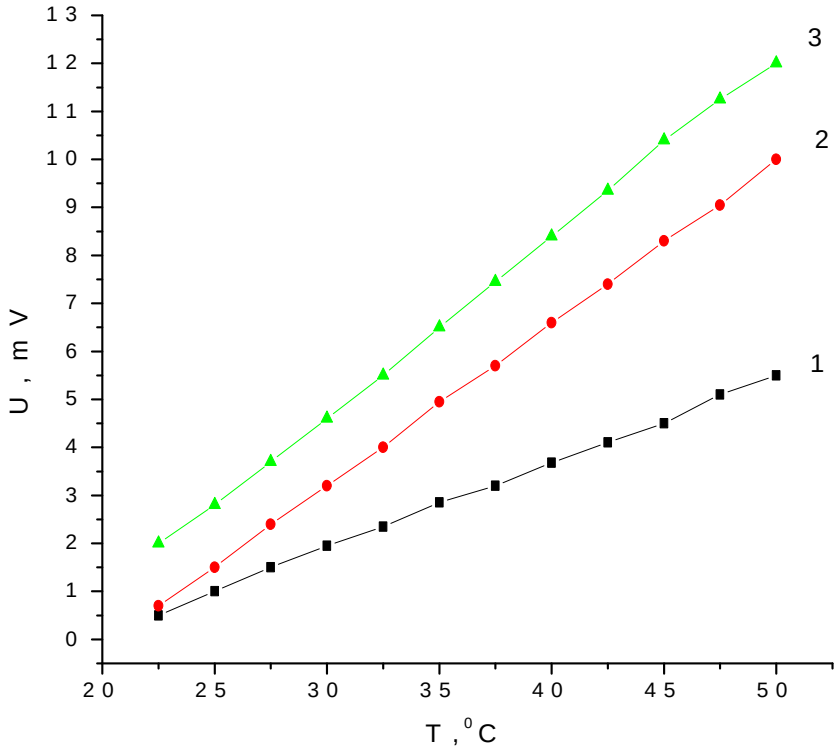

Fig. 27. Temperature dependence of the electric current of the thermocouple.

It is evident that the temperature dependence of signal is linear in a temperature range of 230-270 K. After annealing of the MW, the signal of the microthermocouple is on the order of 2-12 mV in a temperature range of 23-50°C.

9. Microelectrodes

The microelectrode is a glass capillary with a glass-insulated microthermocouple based on Bi_2Te_3 of *n*- and *p*-type conduction placed in it. It serves for removing the biopotentials and measuring the temperature of living organisms and plants. The length of the active part is 5-45 mm; the diameter of the active part is 0.5-1.0 mm, and the area of the contacting region is 50 μm^2.

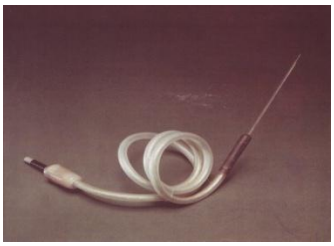

Fig. 28. Microelectrode.

10. Conclusions

- The technique for the preparation of MWs from thermoelectric materials based on PbTe and Bi_2Te_3 by the Ulitovsky method and by the filling of capillaries under an inert gas pressure has been optimized. The highest-quality MWs of lead telluride have been prepared by the second method.
- A technique for the preparation of a bifilar MW based on Bi_2Te_3 using a modified Ulitovsky method has been developed.
- The temperature dependences of the resistivity and thermopower of the MWs in a temperature range of 77-350 K have been measured.
- The thermal efficiency of the MWs has been calculated and compared with the thermal efficiency of bulk samples.
- The PbTe-based MWs were used to prepare IR detectors and injection lasers; the Bi_2Te_3-based MWs were used to prepare a microthermocouple with a high sensitivity and microelectrodes for removing the biopotentials and measuring the local temperature of microorganisms, living organisms, and plants.

References

[1] D.M.Freik, M.A. Galushchak, and L.I. Mezhilovskaya, Fizika i tehnologiya poluprovodnikovyh plenok, L'vov, Vyshcha Shkola, 1988, 152 p.
[2] W. Lu, J. Fang, K.L.Stokes, and J. Lin, J. Am. Chem. Soc., 126, 11798 (2004).
[3] T. Gutsul, A. Nikorich, and A. Todosichuk, Stabilizatsiya oleinovoy kislotoy nanochastits PbTe, poluchennyh metodom HTSPS, 2nd Int. Conf. "Telecommunications, Electronics and Informatics," Proceedins, V.II, Chisinau, 2008, p.279–284.
[4] D.F. Megley, M.P. Dyntu, and S.V. Donu, Osobennosti rosta nitevidnyh kristallov tellurida svintsa olova, International Conference ICT+ „Information and Communication Technologies – 2009", Proceedins, Chisinau, 2009, p.105–107.

[5] D.F. Meglei, V. Kantser, and M. Dantu, Mold. J. Phys. Sci. 2, 2, 177 (2003).
[6] G.F.Taylor. Phys. Rev. 23, 655 (1924).
[7] E.Ya. Badinter, N.R.Berman, et al., Litoy mikroprovod i ego svoystva, Shtiintsa, Kishinev, 1973, 318 p.
[8] A.V. Ulitovskii and N.M. Averin, USSR Author's Certificate 161325, MKI g 03 C 29/-00, Byull. Izobret., 7, 14 (1964)
[9] D. Meglei, Mold. J. Phys. Sci. 9, 70 (2010).
[10] V. Canter, D. Meglei, and A. Rusu, Precedeu de obţinere a microfiorului coaxial, Brevet de inventie no. 2752 , 2005.04.30. BOPI nr. 4/2005.
[11] D. Meglei, M. Dantu, E. Condrea, and A. Rusu, Procedeu de confectionare a microconductorului bifilar. Brevet de inventie h01b 13/06, h01b 3/08 A 2008 0209, 2009.12.22.
[12] V.F. Banar', F.G. Donika, and A. Shkurpelo, Izv. Akad. Nauk MSSR, ser. Fiz.-Tech. Mat. Nauk 3, 66 (1982).
[13] M.P. Dyntu, V.G. Kantser, D.F. Meglei, Int. Semicond. Conf. 19-th Ed., October 9-12, Sinaia, Romania, 109 (1996).
[14] C.S. Evans and J.S. Secly, J. Phys. Suppl. 29, 11-12, 4 (1968).
[15] R. Smith, Poluprovodniki, Mir, Moscow, 1982, 467 p.
[16] T. Moss, G. Barel, and B. Ellis, Poluprovodnikovaya optoelektronika, Mir, Moscow, 1976, 431 p.
[17] Opticheskie svoystva poluprovodnikov A^3B^5, edited by R. Uillardson and A. Bir, Sov. Radio, Moscow, 1970, 488 p.
[18] A. Ambrozyak, Konstruktsiya i tehnologiya poluprovodnikovyh fotoelektricheskih priborov, Sov. Radio, Moscow, 1970, 392 p.